

## Research



**Cite this article:** de Obeso JC, Kelemen PB. 2020 Major element mobility during serpentinization, oxidation and weathering of mantle peridotite at low temperatures. *Phil. Trans. R. Soc. A* **378**: 20180433. <http://dx.doi.org/10.1098/rsta.2018.0433>

Accepted: 2 October 2019

One contribution of 11 to a discussion meeting issue 'Serpentinite in the Earth system'.

**Subject Areas:**

geochemistry, geology

**Keywords:**

serpentinization, thermodynamic modelling, Oman, ophiolite

**Author for correspondence:**

Juan Carlos de Obeso

e-mail: [deobeso@ldeo.columbia.edu](mailto:deobeso@ldeo.columbia.edu)

Electronic supplementary material is available online at <https://doi.org/10.6084/m9.figshare.c.4750601>.

# Major element mobility during serpentinization, oxidation and weathering of mantle peridotite at low temperatures

Juan Carlos de Obeso and Peter B. Kelemen

Lamont-Doherty Earth Observatory, Earth and Environmental Sciences, Columbia University, New York, Palisades, NY 10964, USA

JCO, 0000-0002-9962-8177

Mantle peridotite in Wadi Fins in eastern Oman exhibits three concentric alteration zones with oxide and sulfide mineralogy recording gradients in  $fO_2$  and  $fS_2$  (fugacity) of more than 20 orders of magnitude over 15–20 cm. The black cores of samples (approx. 5 cm in diameter) exhibit incomplete, nearly isochemical serpentinization, with relict primary mantle minerals (olivine, orthopyroxene and clinopyroxene) along with sulfide assemblages (pentlandite/hezlewoodite/bornite) recording low  $fO_2$  and moderate  $fS_2$ . In addition to the black cores, two alteration zones are evident from their colouration in outcrop and hand samples: green and red. These zones exhibit non-isochemical alteration characterized by intergrowths of stevensite/lizardite. All three reaction zones are cut by calcite  $\pm$  serpentine veins, which are most abundant in the outer, red zones, sometimes are flanked by narrow red and/or green zones where they cut the black zones, and thus may be approximately coeval with all three alteration zones. The alteration zones record progressively higher  $fO_2$  recorded by Ni-rich sulfides and iron oxides/hydroxides. These alteration zones lost 20–30% of their initial magnesium content, together with mobilization of iron over short distances from inner green zones into outer red zones, where iron is reprecipitated in goethite intermixed with silicates due to higher  $fO_2$ . Thermodynamic modelling at 60°C and 50 MPa (estimated alteration conditions) reproduces sulfide assemblages,  $fO_2$  changes and Mg and Fe mobility.

This article is part of a discussion meeting issue 'Serpentinite in the Earth system'.

## 1. Introduction

Alteration of mantle peridotite is an important part of the global geochemical cycle. Peridotite minerals, mainly olivine ((Mg,Fe)<sub>2</sub>SiO<sub>4</sub>) and pyroxenes ((Ca,Mg,Fe)<sub>2</sub>Si<sub>2</sub>O<sub>6</sub>), are far from equilibrium in Earth's near-surface conditions, and are altered by aqueous fluids to form hydrated silicates (serpentinization), carbonates (carbonation) and oxides. Serpentinization of seafloor peridotites is a significant sink for water, carbon and sulfur [1–3]. Carbonation of peridotites is an important part of the present carbon cycle (e.g. [3,4]), and could be accelerated to achieve significant capture and storage of anthropogenic carbon emissions [5–7].

In many cases, serpentinization and carbonation of mantle peridotite are inferred to be nearly isochemical, except for the addition of water and carbon dioxide (e.g. [8,9] and references therein), though in detail there could be small changes in major element concentrations (e.g. [10]). Reaction pathways for serpentinization vary, depending on temperature, pressure, fluid composition, fluid/rock ratios and the primary mineralogy of the protolith. Serpentinization at relatively low time-integrated water/rock (W/R) ratios produces strongly reducing conditions [11–13]. The resulting fluids are among the most reduced on Earth, saturated in metal alloys such as awaruite (Ni<sub>2</sub>Fe to Ni<sub>3</sub>Fe), wairauite (CoFe) and native copper (Cu), and sulfides including heazlewoodite (Ni<sub>3</sub>S<sub>2</sub>) and polydymite (Ni<sub>3</sub>S<sub>4</sub>) (e.g. [13,14]). As fluid/rock ratios increase, the alteration system becomes fluid-dominated, resulting in more oxidizing and alkaline conditions that produce opaque mineral assemblages recording variable oxygen fugacity  $f_{O_2}$  (e.g. [1,11,14,15]).

This paper describes the alteration sequence and geochemistry of a suite of pervasively altered mantle peridotites that record variable  $f_{O_2}$  over short distances (10–15 cm) in Wadi Fins in a southeastern exposure of the Samail ophiolite in the Sultanate of Oman. We first describe and present data on the mineralogy and chemistry observed in the Wadi Fins rocks, and then use these data to constrain temperature,  $f_{O_2}$  and fluid fluxes during alteration to provide insights on pervasive alteration processes of mantle peridotites relevant to multiple geological settings.

## 2. Geological setting

The Samail ophiolite along the northeast coast of Oman is among the largest and best-exposed sections of oceanic crust and its underlying mantle in the world (see [16,17] and references therein). It was thrust over adjacent oceanic lithosphere soon after the magmatic formation of oceanic crust at a submarine spreading ridge, and then onto the margin of the Arabian subcontinent in the Late Cretaceous [18–21].

The mantle section of the ophiolite is mainly composed of highly depleted, residual mantle peridotites (mostly harzburgites, e.g. [22–24]), together with 5–15% dunite [25–27], and refertilized lherzolites near the basal thrust [28]. These peridotites are pervasively serpentinized, with serpentine ( $\pm$  brucite) composing approximately 30 wt% in 'fresh' rock to nearly 100% [29,30]. The alteration occurred throughout the history of the ophiolite, beginning near the axis of the oceanic spreading ridges where the Samail ophiolite crust formed (e.g. [31]) and continuing to the present day (e.g. [7,32–34]).

The mantle peridotites were exposed by sub-aerial erosion in the Late Cretaceous. They are locally capped by Late Cretaceous (Maastrichtian) laterites [35,36], and elsewhere by fluvial conglomerates rich in peridotite cobbles. This was followed by a marine transgression, which deposited shallow marine carbonates over a broad region in the Arabian peninsula, including the Qahlah, Simsina and Jafnayn formations [35]. The carbonate cover is particularly extensive in the southeastern section of the ophiolite [35,37]. In this area, outcrops of peridotite are rare and occur only on the bottom of deep canyons like Wadi Tiwi and Wadi Fins where erosion has cut down through the Late Cretaceous unconformity. In Wadi Fins (figure 1), peridotites below the unconformity were altered at low temperatures (approx. 60°C or less) and pressures (50 MPa); based on the thickness of the overlying sediments [30], the observation of abundant millimetre-to-centimetre-scale vugs (cavities in veins terminated with euhedral crystals) indicates that fluid pressure must have been close to lithostatic pressure. Serpentinizing fluids were derived from

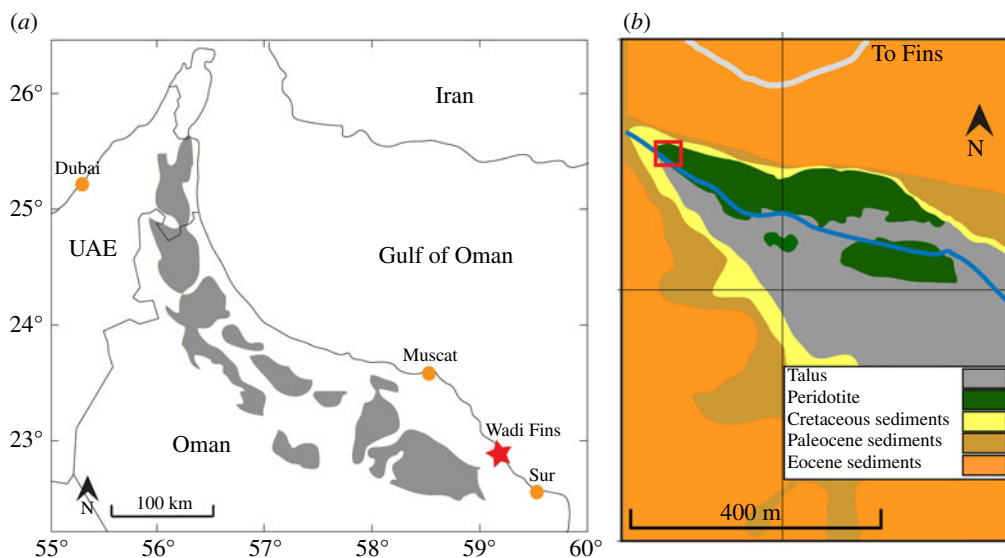


**Figure 1.** (a) Map of the Samail ophiolite after Hanghøj *et al.* [24]. Red star shows the location of Wadi Fins. (b) Geologic map of Wadi Fins compiled from Wyns *et al.* [38], Google Earth data, and field observations. Red square marks the location of the samples described in this study. Map area is between UTM coordinates 2 532 838–2 533 636 m N and 721 824–722 181 m E in zone 40 Q (adapted from de Obeso & Kelemen [30]). (Online version in colour.)

the overlying limestones, providing a source of water, calcium, carbon and silica to the rocks, sufficient to reduce bulk rock MgO/SiO<sub>2</sub> ratios, and form an extensive network of carbonate and serpentine–carbonate veins [30].

### 3. Analytical methods

Analysed samples were collected during the 2013 and 2015 field seasons in Wadi Fins, Oman (UTM 40Q 722503E 2533160N). All samples were collected from an outcrop close to the Cretaceous unconformity (figure 1). This outcrop exhibits concentric halos of alteration with sharp oxidation gradients and an extensive network of carbonate veins (figure 2). Hand samples were subdivided and powdered in alumina in four parts following the visually evident reaction fronts (figure 2): part 1, partially serpentinized cores (black cores); part 2, metasomatically modified peridotite (green zones); part 3, oxidized peridotite (red zones); and part 4, carbonate veins.

Powdered samples were analysed by X-ray diffraction (XRD) at Lamont-Doherty Earth Observatory (LDEO) using an Olympus Terra portable XRD. Diffractograms were analysed using Match! software to identify main minerals.

Major element concentrations and loss on ignition (LOI) of the bulk rocks were measured at LDEO using an Agilent 720 Axial ICP-OES. Concentrations of Fe<sub>2</sub>O<sub>3</sub> were determined from ICP-OES (inductively coupled plasma optical emission spectroscopy) data together with FeO concentrations determined by titration. Trace elements were analysed at LDEO using a VG PlasmaQuad ExCell quadrupole ICP-MS (inductively coupled plasma mass spectrometry) following HNO<sub>3</sub>–HF digestion. Standards and analytical precision are given in the electronic supplementary material, tables S1 (ICP-OES) and S2 (ICP-MS).

Polished thin sections were analysed with a standard petrographic microscope for mineral identification where possible. These thin sections were quantitatively analysed using a five-spectrometer Cameca SX-100 electron microprobe (EMP) at the American Museum of Natural History (AMNH). Calibration information is reported in the electronic supplementary material, table S3. For small opaque minerals that were impossible to identify in reflected light, chemical compositions from EMP were essential for phase identification.

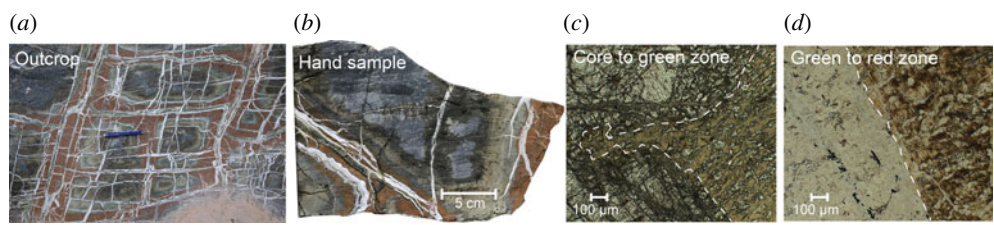


**Figure 2.** Contacts between alteration zones in Wadi Fins, Oman. (a) Peridotite outcrop close to the unconformity with overlying limestones, with sharp reactive fronts in a concentric pattern, and a spatially associated carbonate vein network. Pen for scale. (b) OM15-7 hand sample. (c) Photomicrograph of contact between core and green zone in sample OM15-7. (d) Photomicrograph of contact between green and red zone in sample OM15-7. Photomicrographs in plain polarized light. Dashed white lines emphasize contacts between zones. (Online version in colour.)

## 4. Petrology and mineralogy

Bulk rock chemical compositions for partially serpentinized cores (black cores), metasomatically modified peridotite (green zones) and oxidized peridotite (red zones) are shown in table 1.

### (a) Black cores

The cores of samples OM15-5, OM15-6 and OM15-7 show relict primary minerals (olivine, pyroxene and spinel) both in thin section and in diffractograms, along with abundant serpentine. The major element compositions of the sample cores compared to the average ( $\pm 2\sigma$ ) composition of Oman harzburgite [24] are shown in figure 3 using a volatile-free constant-mass isocon [39]. Isocons are designed to detect concentration changes from the original rock during metasomatism. The isocon on these diagrams is a line that goes through the origin and through concentrations of major/minor elements that are thought to have no relative gain or loss of mass. FeO and SiO<sub>2</sub> are slightly enriched in the cores (approx. 4% relative) close to the upper limits of natural variability (average  $\pm 2\sigma$ ) reported by previous studies [22–24]. This enrichment is complemented by a small depletion (approx. 5% relative) in MgO, with concentrations close to the lower bound of variability. All other major elements are within expected variability (figure 3). Most trace elements measured are similar to the composition of highly depleted harzburgites and are within variability (average  $\pm 2\sigma$ ) reported in the ophiolite [22–24], except for Rb (approx. 270 ppb) with concentrations approximately 10 times higher than the average of published compositions (approx. 30 ppb).

EMP analyses of orthopyroxene (opx), clinopyroxene (cpx) and spinel exhibit small deviations from the composition of these minerals in other Oman harzburgites. Both orthopyroxene and clinopyroxene have low Al and Cr concentrations as well as low Cr# (molar Cr/(Cr + Al)) compared to other Oman locations (figure 4). Spinel has high Mg# (molar Mg/(Mg + Fe<sub>Tot</sub>)) and low Cr#, with compositions towards the fertile end of spinels observed in the ophiolite (figure 4). Average serpentine (Mg# 89.1  $\pm$  2.8, 1 $\sigma$ ) is slightly enriched in iron (with apparent incorporation of Fe<sup>3+</sup> in it) compared to precursor olivine (average Mg# 90.4  $\pm$  0.3) and orthopyroxene (average Mg# 90.1  $\pm$  0.3) (figure 5).

Opaque mineralogy in the cores is dominated by Cr-spinels, plus trace quantities of sulfide minerals. Iron oxides were not detected in OM15-6, while in OM15-5 and OM15-7 magnetite is observed in thin section in trace quantities. Ni-rich pentlandite with an average stoichiometry of (Fe<sub>3.1</sub>Ni<sub>5.9</sub>)S<sub>8</sub> was identified in all samples and is the most abundant sulfide (figure 6). Such high nickel contents are associated with pentlandite/heazlewoodite assemblages [40]. End-member heazlewoodite is observed in one sample, suggesting that intergrowths of these two minerals are present in our samples. Multiple Cu-bearing sulfides occur in the black cores, including chalcocite (Cu<sub>2</sub>S), bornite (Cu<sub>5</sub>FeS<sub>4</sub>) and Cu-bearing pentlandites: samaniite (Cu<sub>2</sub>Fe<sub>5</sub>Ni<sub>2</sub>S<sub>8</sub>) and sugakiite

**Table 1.** Bulk rock compositions of Wadi Fins altered peridotites: bdl, below detection limits of the instrument; FeO\*, oxide total Fe, assuming oxidation state of all Fe to be 2+; LOI, loss on ignition.

	detection limits	OM15-5 red zone	OM15-5 green zone	OM15-5 core	OM15-6 red zone	OM15-6 green zone	OM15-6 core	OM15-7 red zone	OM15-7 green none	OM15-7 core
SiO <sub>2</sub> (wt%)	0.04	39.99	44.81	41.33	39.21	45.54	43.56	38.18	46.43	42.49
TiO <sub>2</sub> (wt%)	0.010	0.02	0.02	0.02	0.02	0.02	0.02	0.01	0.02	0.01
Al <sub>2</sub> O <sub>3</sub> (wt%)	0.09	1.40	1.58	1.13	1.65	1.63	0.98	1.32	1.68	1.12
FeO* <sub>tot</sub> (wt%)	0.07	10.71	6.05	7.67	12.28	6.15	8.25	11.35	5.94	7.82
MnO (wt%)	0.02	0.03	0.03	0.10	0.03	0.03	0.12	0.04	0.03	0.10
MgO (wt%)	0.06	29.18	28.75	39.13	28.60	29.08	39.96	28.00	28.81	37.54
CaO (wt%)	0.07	0.92	2.19	1.01	0.83	2.32	0.99	2.47	1.40	1.12
NaO (wt%)	0.01	0.05	0.04	0.01	0.03	0.03	bdl	0.05	0.09	0.01
K <sub>2</sub> O (wt%)	0.01	0.06	0.10	0.02	0.05	0.09	bdl	0.03	0.06	0.01
Cr <sub>2</sub> O <sub>3</sub> (wt%)	0.00	0.49	0.53	0.33	0.55	0.51	0.33	0.45	0.60	0.35
LOI (wt%)		16.91	15.77	8.55	16.74	16.14	5.92	17.1	16.31	8.23
total		99.74	99.87	99.29	99.98	101.53	100.12	99.02	101.38	98.78
Mg#		0.83	0.89	0.90	0.81	0.89	0.90	0.81	0.90	0.90
FeO (wt%) <sup>a</sup>	0.1	1.9	2.4	5.3	2	1.5	5.5	1.2	1.8	5.1
Fe <sub>2</sub> O <sub>3</sub> (wt%) <sup>b</sup>		9.79	4.06	2.63	11.42	5.16	3.05	11.28	4.60	3.02
Fe <sup>3+</sup> /Fe <sub>Tot</sub>		0.84	0.63	0.33	0.85	0.77	0.36	0.90	0.72	0.37
Cr#		0.19	0.18	0.16	0.18	0.17	0.18	0.19	0.19	0.17

<sup>a</sup>Determined by titration.

<sup>b</sup>Calculated by mass balance from ICP-OES and titration data.

**Table 1.** (Continued.)

	detection limits	OM15-5 red zone	OM15-5 green zone	OM15-5 core	OM15-6 red zone	OM15-6 green zone	OM15-6 core	OM15-7 red zone	OM15-7 green none	OM15-7 core
<i>Trace elements</i>										
B (ppm)	1	40	38	151	39	45	117	37	37	146
Co (ppm)	8	112	133	110	98	139	114	102	138	113
Ni (ppm)	23	2591	2865	2275	2448	2889	2357	2414	3029	2322
Cu (ppm)	5	18	21	15	14	23	22	18	27	14
Zn (ppm)	3	40	48	31	44	42	32	40	44	32
Rb (ppm)	0.05	2	2	0.3	1	2	0.4	1	2	0.3
Sr (ppm)	4	118	110	14	113	132	10	129	124	15
Mo (ppb)	43	313	148	138	262	155	128	283	161	128
Cs (ppb)	5	107	97	37	99	105	38	74	79	34
Ba (ppb)	289	1591	2381	bdl	2748	3543	646	4784	4483	bdl
Gd (ppb)	12	16	19	16	19	19	bdl	14	19	12
Dy (ppb)	16	49	57	42	58	69	33	46	54	34
Er (ppb)	7	48	59	43	65	69	35	51	63	37
Tm (ppb)	9	9	11	bdl	12	13	bdl	bdl	11	bdl
Yb (ppb)	22	78	94	63	95	107	52	76	92	61
Lu (ppb)	3	16	16	12	18	19	10	14	18	12
W (ppb)	12	106	32	278	39	22	16	58	13	27
Pb (ppb)	46	64	bdl	101	bdl	bdl	bdl	bdl	bdl	bdl
Th (ppb)	0.27	0.35	1.41	0.52	0.37	0.93	4.19	0.38	0.31	0.29
U (ppb)	0.68	461	9	0.79	237	26	12	672	16	0.90

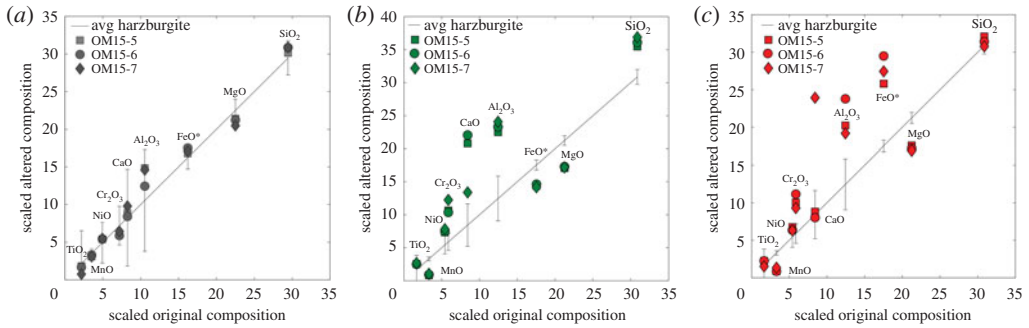


**Figure 3.** Isocon diagram for black cores (a) using average Oman harzburgite (Godard *et al.* [22]; Hanghøj *et al.* [24]; Monnier *et al.* [23]) as the protolith. Green zones (b) and red zones (c) using OM15-6 core as protolith. Elements were scaled to plot within recommended isocon limits. From left to right: TiO<sub>2</sub> ( $\times 100$ ), MnO ( $\times 27$ ), NiO ( $\times 17$ ), Cr<sub>2</sub>O<sub>3</sub> ( $\times 17$ ), Al<sub>2</sub>O<sub>3</sub> ( $\times 12$ ), CaO ( $\times 8$ ), FeO\* ( $\times 2$ ), SiO<sub>2</sub> ( $\times 0.66$ ), MgO ( $\times 0.5$ ). All data are plotted on a volatile-free basis. (Online version in colour.)

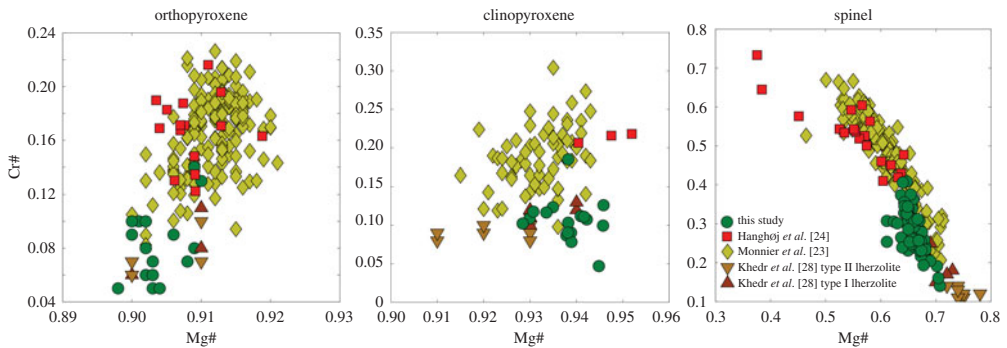


**Figure 4.** Primary mineral Cr# versus Mg# for Wadi Fins partially serpentinized cores. (Online version in colour.)

(Cu,Fe,Ni)<sub>8</sub>S<sub>8</sub>). An obvious mixing trend in figure 6 between pentlandite and chalcocite suggests that these minerals are finely intergrown in these samples. Most sulfides occur along veins filled with serpentine, rather than in spatial association with primary minerals.

## (b) Green zones

The transition from partially serpentinized peridotites (black cores) to the green zones in thin section is very sharp (figure 2), as it is in hand samples and outcrops. Primary minerals are almost completely altered to serpentine. There are abundant bastites (serpentine pseudomorphs replacing pyroxene) as well as fine-grained serpentine with characteristic mesh textures intergrown with a fine-grained mineral with high birefringence, likely talc. Thin sections show a relatively high abundance of microcrystalline, equant to slightly elongated diopside, compared to the black cores. Diffractograms of all samples are noisy with high backgrounds at low  $2\theta$  and some poorly defined, broad peaks suggesting low crystallinity (electronic supplementary material, figure S1). A small broad peak at  $8.8^\circ 2\theta$  in samples OM15-5 and OM15-7 and a larger peak at  $6.2^\circ$  in OM15-6 confirms the presence of clay minerals: montmorillonite and stevensite (Mg-montmorillonite) coexisting with lizardite. The proportions of these end-members are very uniform and close to 1 : 1 (figure 7), which may reflect alternating serpentine and stevensite layers on the scale of the unit cell [41].

The bulk rock composition of green zone samples (figure 3 and table 1) shows enrichments of SiO<sub>2</sub> (approx. 16%), CaO (approx. 150%) and Al<sub>2</sub>O<sub>3</sub> (approx. 80%), and depletion of MgO

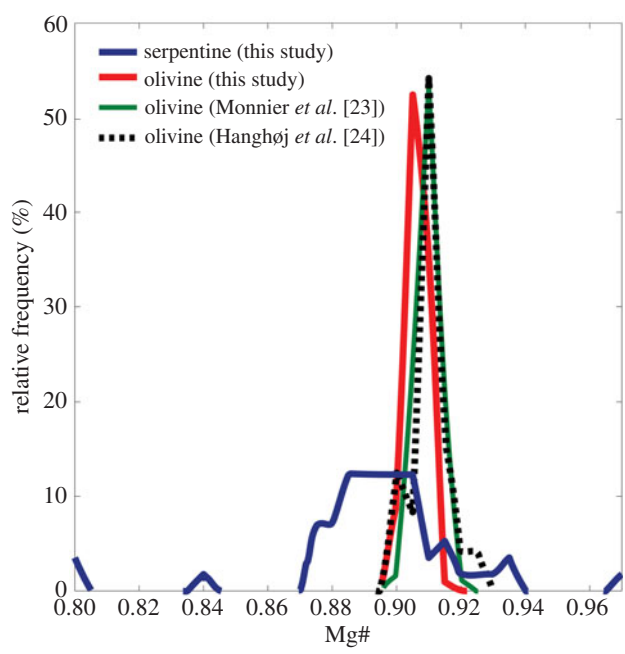


**Figure 5.** Frequency of Mg# in serpentine (blue,  $n = 57$ ) and olivine (red,  $n = 103$ ) from partially serpentinized black cores and literature olivine data: Monnier *et al.* [23] (green,  $n = 171$ ) and Hanghøj *et al.* [24] (black,  $n = 106$ ). (Online version in colour.)

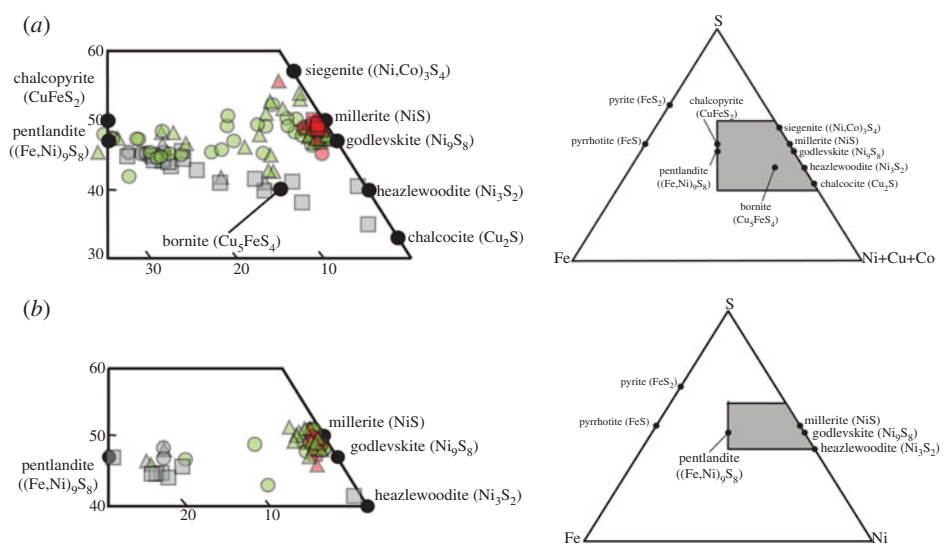


**Figure 6.** Mole fraction ternary diagram of sulfide composition in cores (grey), green zones (green) and red zones (red) in samples OM15-5 (circles), OM15-6 (squares) and OM15-7 (triangles). (a) Fe–Ni–Co–Cu sulfides and (b) Fe–Ni sulfides. (Online version in colour.)

(approx. 20%) and FeO (approx. 17%), compared to the black cores, if constant, volatile-free mass is assumed. The high abundance of diopside in thin section and the relative enrichment in CaO suggest that some of the observed diopside is secondary in origin. Some EMP analyses of serpentine are nearly stoichiometric, with Mg# (avg.  $88.0 \pm 4.5$ ) similar to serpentines in the black

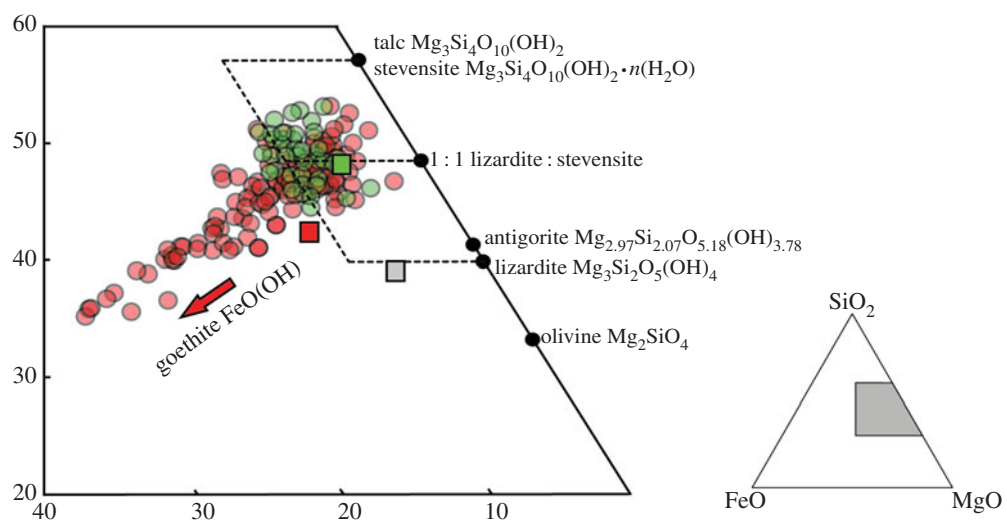


**Figure 7.** Mole fraction Fe–Si–Mg ternary diagram of serpentine and stevensite compositions in green zones and red zones in circles. Squares are whole-rock averages (cores in grey). (Online version in colour.)

cores. Several EMP analyses with low total oxides (73–88 wt%) with molar (Mg + Fe)/Si close to 1 probably represent serpentine intergrown with stevensite, in an assemblage sometimes termed ‘deweylite’ [41,42]. Sr, Rb and U are enriched in the green zones by a factor of 10 compared to the black cores.

Sulfides occur in trace quantities in the green zones. The sulfide assemblages (figure 6) have high Ni/Fe compared to those in the black cores, and have low metal/sulfur ratios, indicating a higher  $f_{O_2}$  than in the black cores. Sulfides include godlevskite ( $Ni_9S_8$ ), millerite (NiS) and siegenite  $(Ni,Co)_3S_4$ . Cu-pentlandite and chalcopyrite ( $CuFeS_2$ ) are the main Cu-bearing sulfides identified in the green zones, and are in close proximity to the black cores. Heazlewoodite is not observed in the green zones.

### (c) Red zones

Like the transition from black to green zones, the transition from green to red zones is sharp in outcrop, hand sample and thin section (figure 2). The red, oxidized zones are characterized by the occurrence of goethite ( $FeO(OH)$ ), lizardite and stevensite as the main minerals identified by XRD. With the assumption of constant, volatile-free mass, when compared to the black zones, bulk rock composition (figure 3 and table 1) does not show significant enrichments in  $SiO_2$  or CaO, unlike the green zones. The isocon diagram does show a significant enrichment in FeO (approx. 50% relative) and  $Al_2O_3$  (approx. 80% relative) and depletion of MgO (approx. 20% relative) compared to the black cores, if constant, volatile-free mass is assumed. Goethite is so finely intergrown with the stevensite/lizardite matrix that no pure microprobe analyses were obtained. Instead, analyses form a mixing line from the stevensite/lizardite assemblages towards goethite (figure 7). Serpentine in the red zones are significantly more iron-rich than the cores and the green zones (avg. Mg#  $74 \pm 11$ ). Sr and Rb have a 10-fold enrichment compared to the black cores, as in the green zones. U in red zones of samples OM15-5 and OM15-7 is up to approximately 600 times more abundant than in the cores. Only Ni sulfides, godlevskite, millerite and siegenite, were identified in the red zones.

### (d) Carbonate and serpentine veins

Veins of carbonate  $\pm$  serpentine are a striking feature of the outcrops (figure 2). These are similar to the veins described by de Obeso & Kelemen [30], from outcrops a few hundred metres

east (downstream) from the sample locality described in this paper. The wider carbonate veins (approx. 1–2 cm) have carbonate, mainly calcite, with minor dolomite bands (approx. 100  $\mu\text{m}$ ) along contacts with altered peridotite. The oxidized, red zones described above usually surround these wider veins. Smaller (less than 1 cm thick) veins composed of pure carbonate minerals (mainly calcite with minor dolomite close to contacts with peridotite) extend from the wider veins into the green zones and less-altered black cores. The branching and cross-cutting veins form right angle intersections in outcrop, creating a pattern of hierarchical fractures that has been associated with volume change during serpentinization and carbonation (e.g. [43–45]).

## 5. Thermodynamic modelling

### (a) Model set-up

Using the petrological and mineralogical constraints described above, we used a modified version of the de Obeso & Kelemen [30] EQ3/6 model [46] of hydrous fluids reacting with peridotite. The model is run at 50 MPa and 60°C, the maximum alteration temperature estimated for Wadi Fins based on clumped isotope data [30]. In addition to major oxides, we included Ni, S and Cu in the model system. For all calculations, we used a modified version of the Klein *et al.* [47] EQ3/6 thermodynamic database. We added stevensite ( $\text{Mg}_3\text{Si}_4\text{O}_{10}(\text{OH})_2 \cdot 6(\text{H}_2\text{O})$ ) to the database using log  $K$  values reported in the electronic supplementary material, table S9. The same database was used to build phase diagrams for the Fe–Ni–Cu–O–S system at 60°C using Geochemist's Workbench v. 12.0.2. Secondary minerals allowed to precipitate along the reaction path are listed in the electronic supplementary material, table S10.

The model has five main stages. In the first, 1 kg of simulated Cretaceous seawater (electronic supplementary material, table S11) is speciated at 25°C using EQ3. In the second stage, the speciated seawater is heated to 60°C and then equilibrated with calcite and quartz in a closed system, to approximate pore water in the  $\text{SiO}_2$ -bearing limestones overlying peridotites in the area. Assumptions regarding source fluid composition are based on the  $^{87}\text{Sr}/^{86}\text{Sr}$  of the calcite veins in our samples.  $^{87}\text{Sr}/^{86}\text{Sr}$  is higher than in the limestone immediately above the unconformity, and higher than in seawater during the time of formation of the unconformity [30], and instead corresponds approximately to the Sr isotope ratio in seawater at the Cretaceous–Palaeocene boundary, and in overlying limestones of that age tens of metres above the unconformity [48]. In the third stage, the resulting fluid reacts with rock with the composition of OM15-6 core using EQ6 with special reactant mode in a titration system at 60°C. (We also ran models in reaction path mode, which yielded very similar results.) The fourth stage models an open system in which the most evolved fluids from the third stage react with secondary minerals precipitated over the reaction path, to simulate fluids flowing through black cores and back into more altered rocks, while reacting with the alteration phases that were precipitated along the stage 3 reaction path. Results from the third and fourth stages of the model are reported as a function of water/rock mass ratios ( $W/R$ ), following the literature convention (e.g. [14,49]). The evolved fluids from stage 4 are finally mixed with initial seawater in stage 5.

### (b) Model results

The results from stage 3 of the model are shown in figure 8. Serpentine is the most abundant mineral along the entire reaction path.  $\text{Fe}^{3+}$  is incorporated into serpentine down to a  $W/R$  ratio of about 4. As  $W/R$  decreases, diopside and stevensite precipitate while some  $\text{Fe}^{2+}$  is incorporated into serpentine. Calcite is predicted in the equilibrium mineral assemblage at  $W/R > 500$ , along with stevensite and serpentine.  $W/R < 10$  is characterized by precipitation of serpentine, magnesite, secondary diopside and minor stevensite. Sulfide and oxide minerals follow changing  $f\text{O}_2$  and  $f\text{S}_2$  as  $W/R$  increases (figure 9). At  $W/R > 800$ , sulfur is oxidized and is present as dissolved sulfate rather than sulfide minerals, and  $f\text{S}_2$  is very low. Millerite is predicted to precipitate when  $W/R$  is between 800 and 10. Chalcopyrite forms at  $W/R > 3$ , whereas the

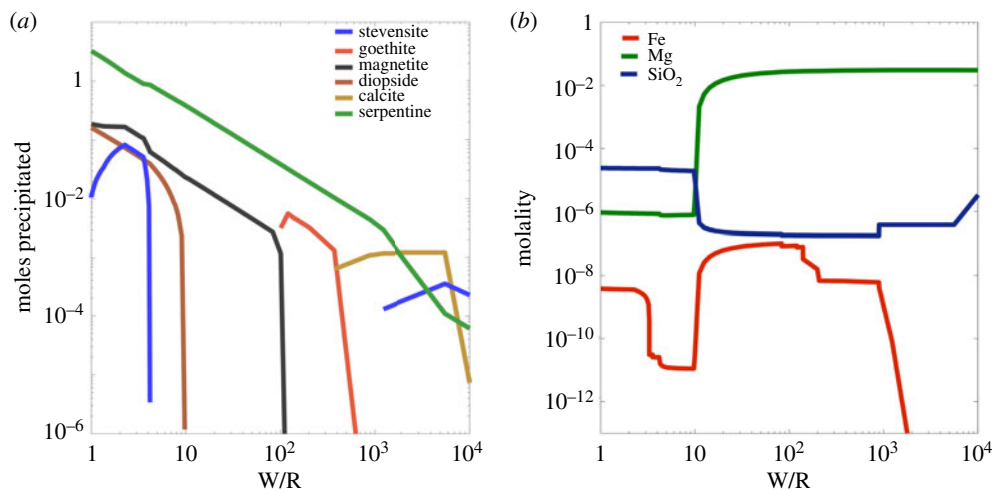


**Figure 8.** Stage 3 model results. (a) Secondary mineralogy and (b) fluid composition as a function of water/rock (W/R). (Online version in colour.)

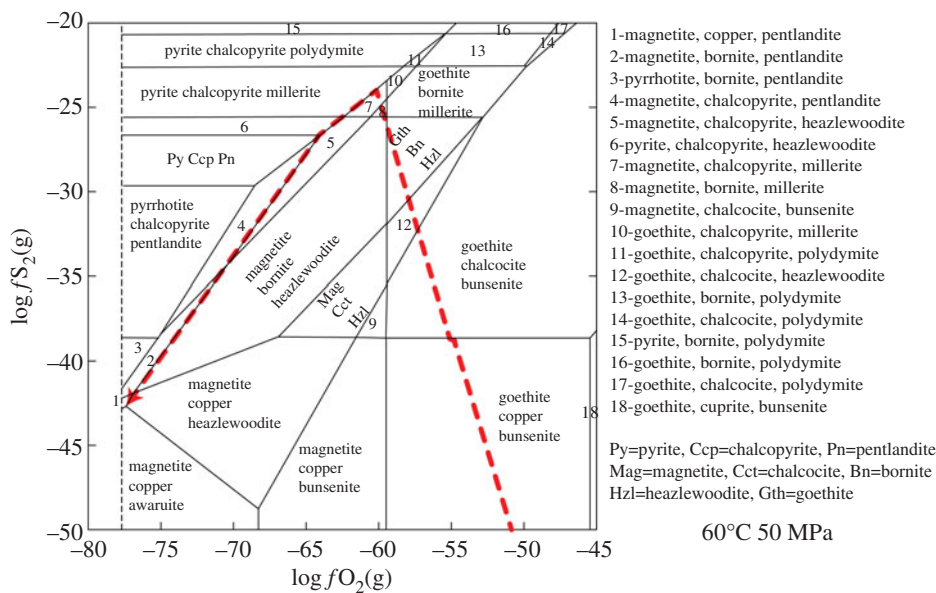


**Figure 9.** Log  $f_{O_2}$ –log  $f_{S_2}$  diagram for calculated sulfide and oxide stabilities at 60°C and 50 MPa in the system Fe–Ni–Cu–O–S. The phase diagram assumes H<sub>2</sub>O activity to be one. All equilibrium constants come from a GWB database customized for sulfide, oxide and alloy minerals constructed using the EQ3/6 database. Red dashed arrow shows results of stage 3 thermodynamic modelling, pointing towards lower W/R. (Online version in colour.)

bornite is precipitated at lower W/R. Pentlandite coexisting with heazlewoodite and bornite is replaced by awaruite at W/R close to 1.

Fe is almost completely insoluble at high W/R, where  $f_{O_2}$  is high. By contrast, iron is mobile in the system at W/R between 1000 and 10, and particularly between 1000 and 100. Fe and Mg are about four orders of magnitude more soluble, and SiO<sub>2</sub> is two orders of magnitude more soluble, above W/R of 10, compared to their solubility at lower W/R. W/R ratios below 10 are characterized by nearly constant fluid composition.

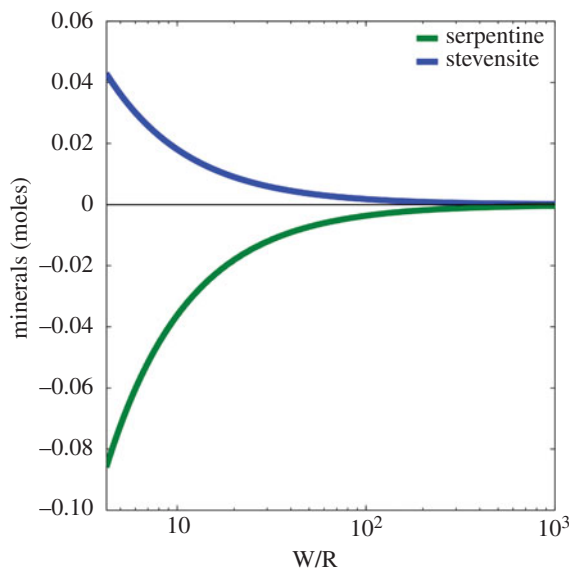


**Figure 10.** Stage 4 model results, illustrating serpentine consumption and stevensite precipitation. (Fe from serpentine is also converted to magnetite in the model reaction). (Online version in colour.)

Stage 4 is characterized by the conversion of serpentine to stevensite. Up to 10% of the stage 3 serpentine reacts to stevensite at  $W/R$  close to 5 (figure 10), and—compared to the final fluid from stage 3—the stage 4 fluid is enriched in Fe (16%) and Mg (64%) and depleted in  $\text{SiO}_2$  (20%). Further reaction of the stage 3 final fluid with stevensite and serpentine results in the formation of progressively more stevensite at the expense of serpentine, enriching the stage 4 mineral assemblage in  $\text{SiO}_2$  (3  $\mu\text{mol}$  of serpentine per kg of water). The final stage 4 fluid, enriched in Fe and Mg (relative to stage 3 evolved fluid), precipitates all its Fe as goethite when mixed with additional, stage 2 pore water in stage 5.

## 6. Discussion

### (a) Petrogenesis of the Wadi Fins protolith

Wadi Fins harzburgites are residues of partial melting and melt extraction, similar to harzburgites from other areas of the ophiolite [22–24] and as depleted as the most depleted abyssal peridotites (e.g. [50–53]). However, spinel Cr# values in Wadi Fins lie within the low end of the field defined by spinels from the Oman harzburgites, some with values as low as  $\text{Cr}\# = 15$  (figure 4). Cr# in opx and cpx are also relatively low, averaging 11 in cpx and 7 in opx. By comparison, pyroxene Cr# in typical Samail harzburgites ranged from 9 to 30 in cpx (avg. 18) and from 8 to 22 in opx (avg. 16). While the low Cr# in these minerals are similar to those in fertile basal lherzolites (11–25 in spinel (avg. 15), 8–11 in cpx (avg. 9) and 6–11 in opx (avg. 8)) [28], average concentrations of Al and Cr in cpx and opx from Wadi Fins are lower than any previously reported concentrations in Samail harzburgites (electronic supplementary material, tables S5 and S6). Temperatures estimated using the Brey & Kohler [54] Ca-in-orthopyroxene and two-pyroxene thermometers, and the Witt-Eickschen & Seck [55] Al-in-orthopyroxene thermometer, suggest that Wadi Fins harzburgites equilibrated at temperatures of approximately 800°C (table 2). Closure temperatures and cooling rates in harzburgites in the Wadi Tayin massif of the Samail ophiolite, the nearest large massif to Wadi Fins, decrease systematically with depth away from the palaeo-Moho [24,56]. This observation, together with low equilibration temperatures in Wadi Fins and low Cr#, suggest that these harzburgites cooled slowly deep in the mantle section, allowing for extensive Al

**Table 2.** Temperatures of Wadi Fins peridotites.

sample	Ca in opx Brey & Kohler [54]			Al in opx Witt-Eickschen & Seck [55]			two pyroxene (BKN)	
	$T$ (°C)	$1\sigma$	$n$	$T$ (°C)	$1\sigma$	$n$	$T$ (°C)	$n$
OM15-6	814.5	42.3	7	778.3	58.9	6	845.3	5
OM15-7	788.8	30.3	9	731.8	44.1	9	880.9	9
OM15-5	861.7	79.8	5	886.1	156.2	4	n.a.	n.a.

transfer from pyroxenes to spinel. Growth of additional spinel during subsolidus cooling and re-equilibration provided a sink for both Al and Cr from pyroxenes.

### (b) Low W/R serpentinization recorded in the black cores

Serpentinization reactions combine ultramafic rocks with hydrous fluid, commonly forming serpentine, brucite, magnetite and hydrogen (see review by Moody [57] and references therein). However, in detail, the mineral products depend on the original protolith, water/rock ratios (W/R), temperature, pressure and fluid composition (e.g. [11,13,47,58–60]). At W/R ratios close to 1,  $\text{Fe}^{2+}$  in mantle silicates is oxidized to form magnetite or  $\text{Fe}^{3+}$ -rich serpentine, producing very low oxygen fugacities ( $f\text{O}_2$ ) in the fluid, leading to dissociation of  $\text{H}_2\text{O}$  to form  $\text{H}_2$  (e.g. [61,62]). While olivine is actively serpentinizing,  $f\text{O}_2$  is buffered to extremely low values by such reactions [60].

In his classic paper, Frost [11] proposed that sulfide–oxide assemblages in the Fe–Ni–S–O–H system record the redox conditions during serpentinization. This approach was further developed and applied by Klein & Bach [14]. More recently, Schwarzenbach *et al.* [13] added copper-bearing sulfides to constrain redox conditions in the Cu–Fe–S–O–H system. Based on this prior work, the Fe–Ni–Cu sulfide assemblages in the cores of Wadi Fins samples, pentlandite–heazlewoodite (figure 6), are characteristic of serpentinization at low W/R. Stage 3 modelling predicts mineral assemblages consistent with the sulfide assemblages in the black cores (heazlewoodite–pentlandite–bornite; figure 9) at  $W/R < 3$ . Phase equilibrium constraints and model calculations indicate that these assemblages formed at extremely low  $f\text{O}_2$ , at or near the dissociation limit for  $\text{H}_2\text{O}$  to  $\text{H}_2$ , together with  $f\text{S}_2$  just above the limits for the stability of native metals (awaruite and copper). The lack of native copper and awaruite in the cores is consistent with low alteration temperatures, as their stability fields in  $f\text{O}_2$  versus  $f\text{S}_2$  space shift to lower fugacities at low temperature, compared to those calculated at higher temperatures in previous studies.

### (c) Non-isochemical behaviour and increased $f\text{O}_2$ in green and red zones

Serpentinization is commonly inferred to be nearly isochemical except for the addition of water ([8,63] and references therein), though this is not always accurate in detail [10,23,64,65]. Addition of  $\text{H}_2\text{O}$ , without substantial removal of other components, together with decreasing density as the mineralogy is transformed from olivine + pyroxene to serpentine  $\pm$  brucite, clays, iron oxides, requires substantial volume increases when compared to the original rock [66,67]. Nearly isochemical alteration is inferred for the partially serpentinized, black cores in Wadi Fins, because their Mg/Si/Fe ratios are similar to average Samail harzburgites and residual peridotites worldwide (e.g. [66,68]). This inference is consistent with the results of our stage 3 thermodynamic models at low W/R, which predict mineral assemblages similar to the black cores, insignificant changes in anhydrous rock composition and volatile-free mass, together with very large increases in the solid volume.

The green and red zones in Wadi Fins correspond to a completely different alteration process, at higher W/R. We can constrain W/R using uranium concentrations. Black cores have

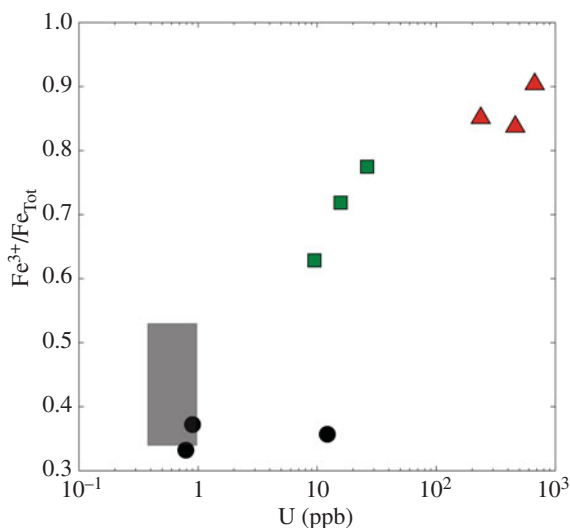


**Figure 11.** Uranium concentrations versus  $\text{Fe}^{3+}/\text{Fe}_{\text{Tot}}$  in Wadi Fins peridotites. Black circles, black cores; green squares, green zones; red triangles, red zones. Symbols are larger than analytical uncertainty. Grey rectangle illustrates the range of U concentration and  $\text{Fe}^{3+}/\text{Fe}_{\text{Tot}}$  reported by Godard *et al.* [22]. (Online version in colour.)

U concentrations similar to Oman harzburgites. By contrast, U concentrations increase dramatically, up to 10× core values in the green zones, and up to 600× core values in the red zones (table 1). This increase correlates with changes in  $\text{Fe}^{3+}/\text{Fe}_{\text{Tot}}$  (figure 11). If almost all of the U is derived from the seawater end-member [69], with approximately 3 ppb U similar to modern seawater [70], then a W/R ratio of 200 or more is necessary to enrich the red zones in Wadi Fins.

The mineralogy and compositions of the green and red zones are not those of a peridotite serpentinized under nearly isochemical conditions, as shown in the isocon diagrams (figure 3). These diagrams suggest pervasive metasomatism, leading to silica-rich and iron-rich compositions in the green and red zones, respectively. This might reflect transitional stages between partially serpentinized peridotites and laterites, such as those observed in Wadi Tiwi [36].

The proportion of  $\text{SiO}_2$  increases sharply (from 45 to 53 wt%, volatile-free) from the black cores to the green zones, and drops back sharply in the red zones to  $\text{SiO}_2$  concentrations similar to those in the black cores. On the other hand, FeO concentration decreases from the black cores to the green zones (from approx. 9 to 7 wt%, volatile-free) and then increases sharply in the oxidized, red zones (to 14 wt%, volatile-free). Assuming immobile  $\text{Al}_2\text{O}_3$  in the isocons for our samples results in a total loss of volatile-free mass of approximately 40% relative. Such a large mass decrease is not supported by field observations or textures at any scale, and is inconsistent with our thermodynamic modelling. Instead, assumptions of (a) constant  $\text{SiO}_2$  and (b) constant, volatile-free mass in the isocon for the red zones yield almost identical results, suggesting that  $\text{SiO}_2$  is relatively immobile. Therefore, we favour the assumption of quasi-constant, volatile-free mass or immobile  $\text{SiO}_2$ , rather than immobile  $\text{Al}_2\text{O}_3$ . The assumption of constant  $\text{SiO}_2$  yields MgO depletion of approximately 25% relative in the green zones and 20% relative in the red zones, compared to the black cores. This is consistent with our stage 4 models, in which MgO is leached out of the rock as serpentine reacts with final stage 3 fluids to form stevensite.

When compared with the black zones, FeO has a depletion of approximately 25% relative in the green zones and an enrichment of approximately 50% relative in the red zones. Our stage 4 model suggests that this may be derived from the mobility of Fe. At low  $f\text{O}_2$ ,  $\text{Fe}^{2+}$  is dissolved from the green zones, transported into the red zones and precipitated as  $\text{Fe}^{3+}$  in goethite due to increasing  $f\text{O}_2$ , as fluids from the cores and green zones mix with oxidizing fluids.

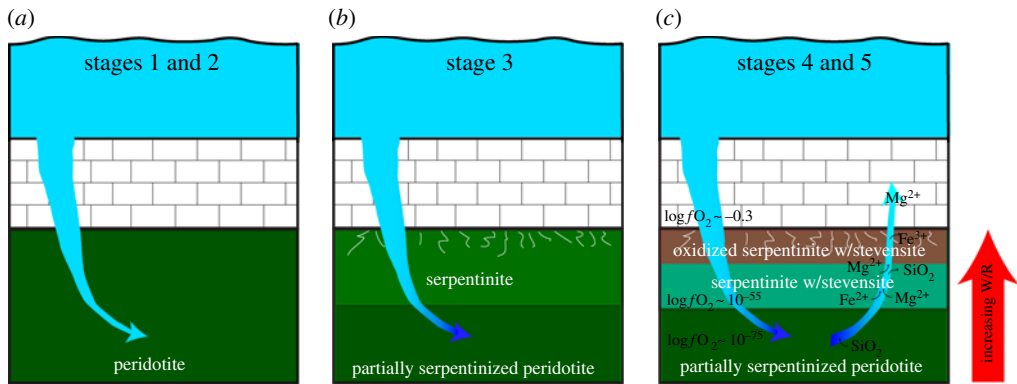


**Figure 12.** Conceptual figure of the alteration process of Wadi Fins peridotites. (a) Seawater infiltrates the overlying limestones. (b) Fluid moves through the peridotite at variable water/rock (W/R) partially serpentinizing the rock at low W/R. (c) Reduced fluid moves away from the partially serpentinized peridotite forming stevensite, leaching Mg and precipitating goethite upon mixture with oxidized fluid. (Online version in colour.)

Further evidence for iron mobility in Wadi Fins can be drawn from the intergrowth of goethite with serpentine in the red zones (figure 7), as well as the presence of iron oxides in the carbonate veins (E. Cooperdock 2018, personal communication). Overall, the remobilization of FeO and leaching of MgO represent a 9% decrease in volatile-free mass (3% mass increase including volatiles) and a 15% increase in solid volume, compared to the protolith represented by the black cores. For comparison, a 100% serpentinized harzburgite under isochemical conditions keeps volatile-free mass constant (approx. 13% mass increase from water) and requires an approximately 45% increase in solid volume [66]. Magnesium loss from highly altered peridotites has been previously inferred from the products of marine weathering [71,72] and has been suggested as a potential mechanism for the formation of ‘deweylite’ assemblages [42].

Peridotites in this area exhibit clear signs of major element mobility during open system weathering resulting in Mg loss and the formation of 1:1 stevensite:lizardite mixtures in the green and red zones, coupled with nearly isochemical alteration of the black cores that preserve partially serpentinized peridotite compositions and mineral assemblages. Variable W/R results in significant changes in mineralogy and  $fO_2$  in different alteration zones (figures 9 and 12). Black cores record highly reducing conditions at  $W/R \sim 1$ , whereas the green and red zones record much higher W/R and  $fO_2$ . This change in  $fO_2$  is evident based on equilibria involving sulfide minerals in the different zones (figure 7) and from the results of thermodynamic modelling (figure 9).

## 7. Conclusion

Altered mantle peridotites in Wadi Fins contain three distinct alteration zones that record a gradient of approximately 20 orders of magnitude in  $fO_2$  and  $fS_2$  in sulfide/oxide mineralogy over a distance of 15–20 cm. The black cores are characterized by pentlandite/heazlewoodite/bornite assemblages, recording very low oxygen fugacities. Such low  $fO_2$  is associated with serpentinization at low W/R [1,11]. The black cores contain relict primary mantle minerals plus alteration products associated with low-temperature, nearly isochemical serpentinization. The green zones surrounding the black cores show pervasive alteration resulting in relatively high  $SiO_2$  concentration and a depletion of MgO and FeO, forming mixtures of stevensite and lizardite. These mixtures are present in the red zones, intergrown with goethite. Thermodynamic modelling suggests that iron and magnesium were mobilized from the green zones following initial serpentinization, via reaction with reduced fluids from core fluids zones. Iron precipitated to form the red zones when the fluids become oxidized, perhaps by mixing with additional

incoming pore water. These mass transfer reactions combine to produce a volatile-free mass loss of 9%, together with a 15% increase in the solid volume, in the green and red zones compared to the black cores. This volume change is significantly less than calculated for isochemical serpentinization of harzburgite (constant volatile-free mass and approx. 45% volume increase). We suspect that the marked zoning seen in this area, which is unusual in the mantle section of the Samail ophiolite, is due to the proximity of the Cretaceous unconformity. The rocks we have studied may be viewed as transitional in some ways between typical, partially serpentinized mantle peridotites in ophiolites and oceanic drill core, on the one hand, and laterites, on the other.

**Data accessibility.** The authors confirm that the data supporting the findings of this study are available within the article and/or its electronic supplementary material. EQ3/6 input files of the thermodynamic modelling are available upon request to the authors.

**Authors' contributions.** J.C.O. processed the samples, acquired the data and built the thermodynamic model with input from P.B.K. Both J.C.O and P.B.K. analysed the data and wrote the paper.

**Competing interests.** We declare we have no competing interests

**Funding.** This work was supported through the Sloan Foundation–Deep Carbon Observatory (grant no. 2014-3-01, Kelemen PI), and the US National Science Foundation (grant no. NSF-EAR-1516300, Kelemen lead PI).

**Acknowledgements.** We thank everyone at the Sultanate of Oman Public Authority for Mining, especially Dr Ali Al Rajhi for facilitating our fieldwork in Oman. D. Nothhaft is thanked for help powdering and cutting samples. A. Fiege, L. Bolge and K. Benedetto are thanked for mentorship and assistance with laboratory work. We are grateful to F. Klein for providing the database used for reaction-path modelling. This article benefits from helpful discussions with E. Cooperdock, A. Templeton, E. Ellison and L. Tweed.

## References

1. Alt JC, Shanks WC. 1998 Sulfur in serpentinized oceanic peridotites: serpentinization processes and microbial sulfate reduction. *J. Geophys. Res.* **103**, 9917. (doi:10.1029/98JB00576)
2. Barnes JD, Sharp ZD. 2006 A chlorine isotope study of DSDP/ODP serpentinized ultramafic rocks: insights into the serpentinization process. *Chem. Geol.* **228**, 246–265. (doi:10.1016/j.chemgeo.2005.10.011)
3. Alt JC *et al.* 2013 The role of serpentinites in cycling of carbon and sulfur: seafloor serpentinization and subduction metamorphism. *Lithos* **178**, 40–54. (doi:10.1016/j.lithos.2012.12.006)
4. Kelemen PB, Manning CE. 2015 Reevaluating carbon fluxes in subduction zones, what goes down, mostly comes up. *Proc. Natl Acad. Sci. USA* **112**, E3997–E4006. (doi:10.1073/pnas.1507889112)
5. Seifritz W. 1990 CO<sub>2</sub> disposal by means of silicates. *Nature* **345**, 486. (doi:10.1038/345486b0)
6. Lackner KS, Wendt CH, Butt DP, Joyce EL, Sharp DH. 1995 Carbon dioxide disposal in carbonate minerals. *Energy* **20**, 1153–1170. (doi:10.1016/0360-5442(95)00071-N)
7. Kelemen PB, Matter JM. 2008 *In situ* carbonation of peridotite for CO<sub>2</sub> storage. *Proc. Natl Acad. Sci. USA* **105**, 17 295–17 300. (doi:10.1073/pnas.0805794105)
8. O'Hanley DS. 1996 *Serpentinites: records of tectonic and petrological history*. New York, NY: Oxford University Press.
9. Kelemen PB, Matter JM, Streit EE, Rudge JF, Curry WB, Blusztajn J. 2011 Rates and mechanisms of mineral carbonation in peridotite: natural processes and recipes for enhanced, *in situ* CO<sub>2</sub> capture and storage. *Annu. Rev. Earth Planet. Sci.* **39**, 545–576. (doi:10.1146/annurev-earth-092010-152509)
10. Malvoisin B. 2015 Mass transfer in the oceanic lithosphere: serpentinization is not isochemical. *Earth Planet. Sci. Lett.* **430**, 75–85. (doi:10.1016/j.epsl.2015.07.043)
11. Frost RB. 1985 On the stability of sulfides, oxides, and native metals in serpentinite. *J. Petrol.* **26**, 31–63. (doi:10.1093/petrology/26.1.31)
12. McCollom TM, Bach W. 2009 Thermodynamic constraints on hydrogen generation during serpentinization of ultramafic rocks. *Geochim. Cosmochim. Acta* **73**, 856–875. (doi:10.1016/j.gca.2008.10.032)
13. Schwarzenbach EM, Gazel E, Caddick MJ. 2014 Hydrothermal processes in partially serpentinized peridotites from Costa Rica: evidence from native copper and complex sulfide assemblages. *Contrib. Mineral. Petrol.* **168**, 1079. (doi:10.1007/s00410-014-1079-2)

14. Klein F, Bach W. 2009 Fe–Ni–Co–O–S phase relations in peridotite–seawater interactions. *J. Petrol.* **50**, 37–59. (doi:10.1093/petrology/egn071)
15. Schwarzenbach EM, Früh-Green GL, Bernasconi SM, Alt JC, Shanks WC, Gaggero L, Crispini L. 2012 Sulfur geochemistry of peridotite-hosted hydrothermal systems: comparing the Ligurian ophiolites with oceanic serpentinites. *Geochim. Cosmochim. Acta* **91**, 283–305. (doi:10.1016/j.gca.2012.05.021)
16. Coleman RG. 1977 Geologic, tectonic, and petrologic nature of four ophiolites. In *Ophiolites: ancient oceanic lithosphere?*, pp. 159–198. Berlin, Germany: Springer.
17. Lippard SJ, Shelton AW, Gass IG. 1986 The geological background. *The ophiolite of northern Oman*. Geological Society, London, Memoirs, vol. 11, pp. 1–16. London, UK: Geological Society. (doi:10.1144/GSL.MEM.1986.011.01.01)
18. Hacker BR, Mosenfelder JL, Gnos E. 1996 Rapid emplacement of the Oman ophiolite: thermal and geochronologic constraints. *Tectonics* **15**, 1230–1247. (doi:10.1029/96TC01973)
19. Nicolas A, Boudier F, Ildefonse B, Ball E. 2000 Accretion of Oman and United Arab Emirates ophiolite – discussion of a new structural map. *Mar. Geophys. Res.* **21**, 147–179. (doi:10.1023/A:1026769727917)
20. Rioux M, Bowring S, Kelemen PB, Gordon S, Miller R, Dudás F. 2013 Tectonic development of the Samail ophiolite: high-precision U–Pb zircon geochronology and Sm–Nd isotopic constraints on crustal growth and emplacement. *J. Geophys. Res. Solid Earth* **118**, 2085–2101. (doi:10.1002/jgrb.50139)
21. Warren CJ, Parrish RR, Waters DJ, Searle MP. 2005 Dating the geologic history of Oman’s Semail ophiolite: insights from U–Pb geochronology. *Contrib. Mineral. Petrol.* **150**, 403–422. (doi:10.1007/s00410-005-0028-5)
22. Godard M, Jouselin D, Bodinier J-L. 2000 Relationships between geochemistry and structure beneath a palaeo-spreading centre: a study of the mantle section in the Oman ophiolite. *Earth Planet. Sci. Lett.* **180**, 133–148. (doi:10.1016/S0012-821X(00)00149-7)
23. Monnier C, Girardeau J, Le Mée L, Polvé M. 2006 Along-ridge petrological segmentation of the mantle in the Oman ophiolite. *Geochem. Geophys. Geosyst.* **7**, Q11008. (doi:10.1029/2006GC001320)
24. Hanghøj K, Kelemen PB, Hassler D, Godard M. 2010 Composition and genesis of depleted mantle peridotites from the Wadi Tayin massif, Oman ophiolite; major and trace element geochemistry, and Os isotope and PGE systematics. *J. Petrol.* **51**, 201–227. (doi:10.1093/petrology/egp077)
25. Boudier F, Coleman RG. 1981 Cross section through the peridotite in the Samail ophiolite, southeastern Oman mountains. *J. Geophys. Res.* **86**, 2573. (doi:10.1029/JB086iB04p02573)
26. Kelemen PB, Braun MG, Hirth G. 2000 Spatial distribution of melt conduits in the mantle beneath oceanic spreading ridges: observations from the Ingalls and Oman ophiolites. *Geochem. Geophys. Geosyst.* **1**, 1005. (doi:10.1029/1999GC000012)
27. Braun MG, Kelemen PB. 2002 Dunite distribution in the Oman ophiolite: implications for melt flux through porous dunite conduits. *Geochem. Geophys. Geosyst.* **3**, 1–21. (doi:10.1029/2001GC000289)
28. Khedr MZ, Arai S, Python M, Tamura A. 2014 Chemical variations of abyssal peridotites in the central Oman ophiolite: evidence of oceanic mantle heterogeneity. *Gondwana Res.* **25**, 1242–1262. (doi:10.1016/J.GR.2013.05.010)
29. Boudier F, Baronnet A, Mainprice D. 2010 Serpentine mineral replacements of natural olivine and their seismic implications: oceanic lizardite versus subduction-related antigorite. *J. Petrol.* **51**, 495–512. (doi:10.1093/petrology/egp049)
30. de Obeso JC, Kelemen PB. 2018 Fluid rock interactions on residual mantle peridotites overlain by shallow oceanic limestones: insights from Wadi Fins, Sultanate of Oman. *Chem. Geol.* **498**, 139–149. (doi:10.1016/J.CHEMGEO.2018.09.022)
31. Gregory RT, Taylor HP. 1981 An oxygen isotope profile in a section of Cretaceous oceanic crust, Samail ophiolite, Oman: evidence for  $\delta^{18}\text{O}$  buffering of the oceans by deep (>5 km) seawater–hydrothermal circulation at mid-ocean ridges. *J. Geophys. Res.* **86**, 2737–2755. (doi:10.1029/JB086iB04p02737)
32. Neal C, Stanger G. 1985 Past and present serpentinization of ultramafic rocks: an example from the Semail ophiolite nappe of northern Oman. In *The chemistry of weathering* (ed. J Drewer), pp. 249–275. Dordrecht, The Netherlands: Reidel.

33. Clark ID, Fontes J-C. 1990 Paleoclimatic reconstruction in northern Oman based on carbonates from hyperalkaline groundwaters. *Quat. Res.* **33**, 320–336. (doi:10.1016/0033-5894(90)90059-T)
34. Mervine EM, Humphris SE, Sims KWW, Kelemen PB, Jenkins WJ. 2014 Carbonation rates of peridotite in the Samail ophiolite, Sultanate of Oman, constrained through <sup>14</sup>C dating and stable isotopes. *Geochim. Cosmochim. Acta* **126**, 371–397. (doi:10.1016/j.gca.2013.11.007)
35. Nolan SC, Skelton PW, Clissold BP, Smewing JD. 1990 Maastrichtian to early Tertiary stratigraphy and palaeogeography of the Central and Northern Oman Mountains. *Geol. Soc. Lond. Spec. Publ.* **49**, 495–519. (doi:10.1144/GSL.SP.1992.049.01.31)
36. Al-Khribash S. 2015 Genesis and mineralogical classification of Ni-laterites, Oman Mountains. *Ore Geol. Rev.* **65**, 199–212. (doi:10.1016/j.oregeorev.2014.09.022)
37. Schlüter M, Steuber T, Parente M, Mutterlose J. 2008 Evolution of a Maastrichtian–Paleocene tropical shallow-water carbonate platform (Qalhat, NE Oman). *Facies* **54**, 513–527. (doi:10.1007/s10347-008-0150-8)
38. Wyns R, Bechennec F, Le Meteour J, Roger J. 1992 *Geologic map of Tiwi. Muscat, Oman, Ministry of Petroleum and Minerals, Directorate General of Minerals, Sultanate of Oman*. Wallmann.
39. Grant JA. 1986 The isocon diagram; a simple solution to Gresens' equation for metasomatic alteration. *Econ. Geol.* **81**, 1976–1982. (doi:10.2113/gsecongeo.81.8.1976)
40. Harris DC, Nickel EH. 1972 Pentlandite compositions and associations in some mineral deposits. *Can. Mineral.* **11**, 861–878.
41. Faust G, Fahey J. 1962 *The serpentine-group minerals*. Geological Survey Professional Paper 384-A. Washington, DC: US Government Printing Office.
42. Beinlich A, Austrheim H, Glodny J, Erambert M, Andersen TB. 2010 CO<sub>2</sub> sequestration and extreme Mg depletion in serpentinized peridotite clasts from the Devonian Solund basin, SW-Norway. *Geochim. Cosmochim. Acta* **74**, 6935–6964. (doi:10.1016/j.gca.2010.07.027)
43. Iyer K, Jamtveit B, Mathiesen J, Malthesorensen A, Feder J. 2008 Reaction-assisted hierarchical fracturing during serpentinization. *Earth Planet. Sci. Lett.* **267**, 503–516. (doi:10.1016/j.epsl.2007.11.060)
44. Kelemen PB, Hirth G. 2012 Reaction-driven cracking during retrograde metamorphism: olivine hydration and carbonation. *Earth Planet. Sci. Lett.* **345–348**, 81–89. (doi:10.1016/j.epsl.2012.06.018)
45. O'Hanley DS. 1992 Solution to the volume problem in serpentinization. *Geology* **20**, 705. (doi:10.1130/0091-7613(1992)020<0705:STTVPI>2.3.CO;2)
46. Wolery TW, Jarek RL. 2003 *Software user's manual, EQ3/6*, version 8.0. Prepared by Sandia National Laboratories, for USDOE, Office of Civilian Radioactive Waste Management, Office of Repository Development.
47. Klein F, Bach W, Jöns N, McCollom T, Moskowitz B, Berquó TS. 2009 Iron partitioning and hydrogen generation during serpentinization of abyssal peridotites from 15°N on the Mid-Atlantic Ridge. *Geochim. Cosmochim. Acta* **73**, 6868–6893. (doi:10.1016/j.gca.2009.08.021)
48. McArthur JM, Howarth RJ, Bailey TR. 2001 Strontium isotope stratigraphy: LOWESS version 3: best fit to the marine Sr-isotope curve for 0–509 Ma and accompanying look-up table for deriving numerical age. *J. Geol.* **109**, 155–170. (doi:10.1086/319243)
49. Palandri JL, Reed MH. 2004 Geochemical models of metasomatism in ultramafic systems: serpentinization, rodingitization, and sea floor carbonate chimney precipitation. *Geochim. Cosmochim. Acta* **68**, 1115–1133. (doi:10.1016/j.gca.2003.08.006)
50. Paulick H, Bach W, Godard M, De Hoog JCM, Suhr G, Harvey J. 2006 Geochemistry of abyssal peridotites (Mid-Atlantic Ridge, 15°20'N, ODP Leg 209): implications for fluid/rock interaction in slow spreading environments. *Chem. Geol.* **234**, 179–210. (doi:10.1016/j.chemgeo.2006.04.011)
51. Bodinier J-L, Godard M. 2007 2.04 - Orogenic, ophiolitic, and abyssal peridotites. In *Treatise on geochemistry* (eds HD Holland, KK Turekian), vol. 2, pp. 1–73 Oxford, UK: Pergamon. (doi:10.1016/B0-08-043751-6/02004-1)
52. Godard M, Lagabriele Y, Alard O, Harvey J. 2008 Geochemistry of the highly depleted peridotites drilled at ODP sites 1272 and 1274 (Fifteen-Twenty Fracture Zone, Mid-Atlantic Ridge): implications for mantle dynamics beneath a slow spreading ridge. *Earth Planet. Sci. Lett.* **267**, 410–425. (doi:10.1016/j.epsl.2007.11.058)

53. Niu Y. 2004 Bulk-rock major and trace element compositions of abyssal peridotites: implications for mantle melting, melt extraction and post-melting processes beneath mid-ocean ridges. *J. Petrol.* **45**, 2423–2458. (doi:10.1093/petrology/egh068)
54. Brey GP, Kohler T. 1990 Geothermobarometry in four-phase lherzolites II. New thermobarometers, and practical assessment of existing thermobarometers. *J. Petrol.* **31**, 1353–1378. (doi:10.1093/petrology/31.6.1353)
55. Witt-Eickschen G, Seck HA. 1991 Solubility of Ca and Al in orthopyroxene from spinel peridotite: an improved version of an empirical geothermometer. *Contrib. Mineral. Petrol.* **106**, 431–439. (doi:10.1007/BF00321986)
56. Dygert N, Kelemen PB, Liang Y. 2017 Spatial variations in cooling rate in the mantle section of the Samail ophiolite in Oman: implications for formation of lithosphere at mid-ocean ridges. *Earth Planet. Sci. Lett.* **465**, 134–144. (doi:10.1016/j.epsl.2017.02.038)
57. Moody JB. 1976 Serpentinization: a review. *Lithos* **9**, 125–138. (doi:10.1016/0024-4937(76)90030-X)
58. Bach W, Garrido CJ, Paulick H, Harvey J, Rosner M. 2004 Seawater–peridotite interactions: first insights from ODP Leg 209, MAR 15°N. *Geochem. Geophys. Geosyst.* **5**, Q09F26. (doi:10.1029/2004GC000744)
59. Klein F, Bach W, Humphris SE, Kahl W-A, Jöns N, Moskowitcz B, Berquó TS. 2014 Magnetite in seafloor serpentinite—some like it hot. *Geology* **42**, 135–138. (doi:10.1130/g35068.1)
60. Frost RB, Beard JS. 2007 On silica activity and serpentinization. *J. Petrol.* **48**, 1351–1368. (doi:10.1093/petrology/egm021)
61. Bach W, Klein F. 2009 The petrology of seafloor rodingites: insights from geochemical reaction path modeling. *Lithos* **112**, 103–117. (doi:10.1016/j.lithos.2008.10.022)
62. Sleep NH, Meibom A, Fridriksson T, Coleman RG, Bird DK. 2004 H<sub>2</sub>-rich fluids from serpentinization: geochemical and biotic implications. *Proc. Natl Acad. Sci. USA* **101**, 12 818–12 823. (doi:10.1073/pnas.0405289101)
63. Shervais JW, Kolesar P, Andreassen K. 2005 A field and chemical study of serpentinization—Stonyford, California: chemical flux and mass balance. *Int. Geol. Rev.* **47**, 1–23. (doi:10.2747/0020-6814.47.1.1)
64. Merino E, Canals A. 2011 Spontaneous transition of replacive to displacive growth of dolomite in burial dolomitization, and of serpentine in serpentinization. In *AGU Fall Meeting, San Francisco*, Abstract T41B-04.
65. Merino E. 2013 Kinetic-rheological insights uncovered by the self-accelerating brucite-for-periclase replacement—but only if adjusted on volume. The blind spot of geochemists. In *AGU Fall Meeting, San Francisco*, Abstract MR33B-2317.
66. Coleman RG, Keith TE. 1971 A chemical study of serpentinization—Burro Mountain, California. *J. Petrol.* **12**, 311–328. (doi:10.1093/petrology/12.2.311)
67. Macdonald AH, Fyfe WS. 1985 Rate of serpentinization in seafloor environments. *Tectonophysics* **116**, 123–135. (doi:10.1016/0040-1951(85)90225-2)
68. Falk ES, Kelemen PB. 2015 Geochemistry and petrology of listvenite in the Samail ophiolite, Sultanate of Oman: complete carbonation of peridotite during ophiolite emplacement. *Geochim. Cosmochim. Acta* **160**, 70–90. (doi:10.1016/j.gca.2015.03.014)
69. Deschamps F, Godard M, Guillot S, Hattori KH. 2013 Geochemistry of subduction zone serpentinites: a review. *Lithos* **178**, 96–127. (doi:10.1016/j.lithos.2013.05.019)
70. Owens SA, Buesseler KO, Sims KWW. 2011 Re-evaluating the <sup>238</sup>U–salinity relationship in seawater: implications for the <sup>238</sup>U–<sup>234</sup>Th disequilibrium method. *Mar. Chem.* **127**, 31–39. (doi:10.1016/J.MARCHEM.2011.07.005)
71. Snow JE, Dick HJB. 1995 Pervasive magnesium loss by marine weathering of peridotite. *Geochim. Cosmochim. Acta* **59**, 4219–4235. (doi:10.1016/0016-7037(95)00239-V)
72. Milliken KL, Lynch FL, Seifert KE. 1996 Marine weathering of serpentinites and serpentinite breccias, Sites 897 and 899, Iberia Abyssal Plain. In *Proc. Ocean Drilling Program Scientific Results*, vol. 149, pp. 529–540. College Station, TX: Ocean Drilling Program. (doi:10.2973/odp.proc.sr.149.222.1996)